Introducing density variation and pressure in thermodynamically self-consistent continuum phase-change models including phase-field

M. J. Welland* and N. Ofori-Opoku
Canadian Nuclear Laboratories, Chalk River, Ontario, Canada

(Received 16 October 2021; revised 12 January 2022; accepted 25 March 2022; published 28 April 2022)

We present a thermodynamically self-consistent method to introduce dilation/density variation in continuum-scale phase-change models. Dilation incurs a pressure response via a hyperelastic contribution to the free energy that generalizes the lattice constraint. The dilation is represented entirely by species concentrations and permits composition, temperature, and phase-dependent specific volumes in a robust form. The impact of this approach is compared with the common assumption of the lattice constraint through demonstrative Stefan and phase-field models applied to the equilibrium of a Ni-Cu nanoparticle in equilibrium with its melt. Furthermore, the effect of phase and composition-dependent specific volume is explored in free dendritic growth behavior.

DOI: 10.1103/PhysRevMaterials.6.043805

I. INTRODUCTION

Computational simulation of phase-change and microstructure evolution on the continuum scale is a powerful and versatile tool to robustly capture complex interface morphologies, kinetic effects, and the perturbation of bulk thermodynamics by interface energy. Advanced computational resources have led to the application of these tools across a range of fields from climate modeling [1] to biology [2,3] and material science [4–8]. Despite their pervasiveness, these models typically assume the density of phases to be constant, a troubling assumption considering a key phenomenon is the emergence of capillary pressure/elastic dilation and the ensuing departure from bulk thermodynamic equilibrium [9–14]. The extension of constant density to multiple coexisting phases is more troublesome still, as this is generally not the case, and likewise the assumption that all species have equivalent specific volumes.

In this paper, we develop a relatively simple approach suitable for sharp and diffuse interface models such that density change and capillary pressure emerge naturally. The model couples phase change with mass transport while relaxing the lattice constraint and expressing the model in an Eulerian frame of reference. Unknown variables are concentrations of all species in the Eulerian frame, i.e., with respect to a reference volume. The total concentration of species, weighted by their specific volumes, is equated to the local state of elastic dilation/compression. This dilation is associated with a hydrostatic pressure which replaces the lattice constraint while permitting variation in density. Further, the pressure is directly related to thermodynamic driving forces for mass transport and phase change, e.g., via the Grand potential formulation. This paper is an expanded discussion of the companion letter [15].

Alternative methods of including density variation during phase change, notably in Stefan models, generally assume dilute systems in which the density of the phase is approximated to not rely on the concentration of the dilute, diffusing species [16]. This paper does not require a dilute limit for diffusing species nor any restrictions on composition-dependent densification. This is an approach to introducing density variation in phase-field models with clear thermodynamic implications.

This model employs hydrostatic pressure to drive mass transport with diffusive dynamics and does not consider either bulk flow or shear stresses. As such, it applies to quasistatic fluid-fluid simulations or a solid with a high creep rate. However, the representation of dilation is fundamental to fluid dynamics and full elastic treatment, and so this paper may underpin developments in future work. The Grand potential formulation for coexisting phases is employed to control implicit interfacial energy contributions from the bulk phases [10,17].

The model applies to a range of continuum-scale simulations, including sharp interface models [16], level-set methods, and phase-field models [8,18,19]. The sharp interface application results in a generalization of the Stefan model, increasing its range of applicability.

The use of an elastic response to generalize the lattice constraint has been preliminarily explored in the context of phase-field models in previous works [17,19–21]. In this paper, we formalize, expand, and examine the model and its predictions in detail. Reformulation of the approach using the chemical potential as the dependent variable is also presented. The approach is compared with formulations based on the lattice constraint theoretically, identifying additional terms and their interpretation, and quantitatively through numerical experimentation. The model is shown to expand on the lattice constraint case even in the simple case of constant phase volumes and specific volumes due to the additional degree of freedom introduced.

This paper proceeds by first establishing the thermodynamic model for a single phase in the material frame, followed

*Michael.Welland@cnl.ca

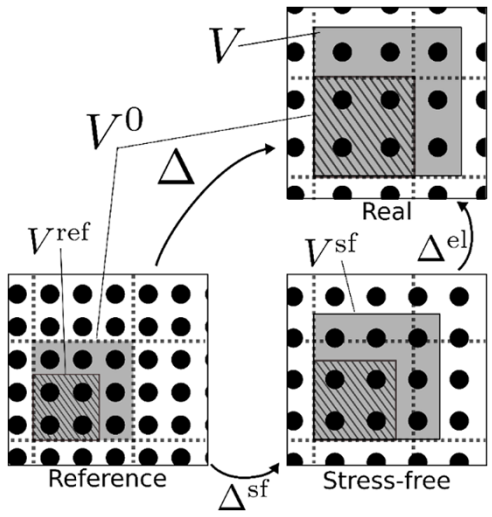

FIG. 1. The total dilation is envisioned as occurring via an intermediate stress-free configuration. The shaded box dilates from V^0, the discretization volume, to the real volume V. The hatched box undergoes approximately the same dilations starting from V^{ref} to V^0. The concentration of particles in V^0 in the real configuration is related to the total dilation.

by the expression in the Eulerian frame. The multiphase model is then established and compared with models that employ the lattice constraint and classical theory. Discussion is facilitated by demonstrative potentials; however, the underpinning theory is generally applicable to arbitrary thermodynamic potential and conducive to expression in software that can exploit symbolic logic to derive thermodynamic quantities for less programming overhead.

II. MODEL DEVELOPMENT

In the ensuing discussion, brackets are used to group terms, and parentheses denote function arguments. A prime superscript denotes quantities without consideration of elastic effects such as those used in models which rely on the lattice constraint.

A. Representation of dilation through concentration

The proposed approach links local species concentration to an elastic dilation which necessitates separating elastic dilation from other phenomena which incur eigenstrains (stress free). This is accomplished through multiplicative decomposition in which the deformation of the material is envisaged as a sequence of transformations from a reference configuration discretized by the volume element V^0 to the current configurations via an intermediate step, as shown schematically in Fig. 1 [22]. The reference configuration is the material without any dilations, while the real configuration is the observable state of the material in which simulations occur. The intermediate stress-free configuration is envisioned as the result of *elastic destressing* from the real configuration. Thus, any phenomena which incur stress-free strains, such as interdiffusion of species with differing specific volumes, thermal expansion, or piezoeffects, but excluding phase change, deform the material from the reference to the stress-free configuration which is then elastically stressed to its real configuration. Multiplicative decomposition then states that the total dilation $\Delta = \Delta^{\mathrm{el}}\Delta^{\mathrm{sf}}$ is the product of the stress-free Δ^{sf} and elastic Δ^{el} dilations. In Fig. 1, the material (Lagrangian) frame is indicated by the array of dots and the Eulerian frame by the grid.

Two infinitesimal parcels of material are considered undergoing the same deformation. The shaded region deforms according to

$$V^0 \to V^{\mathrm{sf}} \to V, \tag{1}$$

while the hatched region, a subset of the shaded one, follows

$$V^{\mathrm{ref}} \to \bar{V}^{\mathrm{sf}} \to V^0. \tag{2}$$

The shaded parcel encloses n_i particles. Since the volume is a homogenous function of species abundance, one can define the specific volume $v_i = \frac{\partial V}{\partial n_i}$, such that $V = \sum_i v_i n_i$, and similarly for the stress-free volume $V^{\mathrm{sf}} = \sum_i n_i v_i^{\mathrm{sf}}$ and the reference volume $V^0 = \sum_i n_i v_i^0$, with specific volumes v_i^{sf} and v_i^0 defined similarly.

The hatched parcel is supposed to contain $\check{n}_i$ particles. Since the hatched parcel is a subset of the shaded one, which is itself arbitrarily small, it is reasonable to assume the dilations and specific volumes are approximately equal. From this, we can identify the dynamic variable of concentration $c_i = \frac{\check{n}_i}{V^0} \approx \frac{n_i}{V}$. Since $V^{\mathrm{ref}} \approx \sum_i \check{n}_i v_i^0$, we can write the dilations

$$\Delta = \frac{V}{V^0} \approx \frac{V^0}{V^{\mathrm{ref}}} = \frac{1}{\sum_i c_i v_i^0}, \tag{3}$$

$$\Delta^{\mathrm{el}} = \frac{V}{V^{\mathrm{sf}}} \approx \frac{V^0}{\bar{V}^{\mathrm{sf}}} = \frac{1}{\sum_i c_i v_i^{\mathrm{sf}}}, \tag{4}$$

where it is noted that $\check{n}_i$ does not appear and is subsequently disregarded from the remainder of this paper.

The limits of the assumption of equal dilations may be explored by considering the shaded region is dilated as $V = V^0\Delta$, while the hatched region dilates by a slightly different factor $V^0 = V^{\mathrm{ref}}[\Delta + d\Delta]$. The requirement $\frac{V}{V^0} \approx \frac{V^0}{V^{\mathrm{ref}}}$ is true if $1 \approx 1 + \frac{\mathrm{d}\Delta}{\Delta}$, and therefore, $\frac{d\Delta}{\Delta} \ll 1$. In turn, this may be related to the gradient of dilation $d\Delta \approx \nabla\Delta V^0$, such that the condition becomes $\frac{\nabla\Delta}{\Delta} V^0 \ll 1$. The validity of this assumption is therefore related to the gradient of the deformation rather than its magnitude; however, large gradients can be handled by shrinking the discretization volume, which is likely already small to resolve the gradient.

The expressions in Eqs. (3) and (4) are worthy of further discussion, as they are the keys to this paper. These equations imply that the state of dilation may be entirely represented by the specific volumes and concentrations of species defined by an Eulerian frame of reference. The explicit volume has not been eliminated from the system and indeed plays a critical role in the ensuing thermodynamic discussion. Rather, this derivation shows that the instantaneous value of dilation may be approximated by the concentration of all species. The approximation is appropriate for typical dilations since the control volumes are arbitrarily small but may fail under extreme strain rates/gradients where thermodynamic equilibration within the control volume is not appropriate.

Initially, it may appear that information about the system has been lost, for example, if the total system expands in size. However, in the Eulerian frame, it is instead represented by the extent of the material over the Eulerian mesh, i.e., whereas in the material frame dilation of a parcel of material is represented by a change in V, dilation in an Eulerian frame implies the movement of mass from the element to adjacent elements or through the boundary of the domain.

B. Thermodynamic model

Ideally, the volume/pressure dependence of a thermodynamic potential would be available. However, typically, only the Gibbs free energy as a function of the composition $G'(n_i, P = P^0)$ is available. One may add elastic dependence to consider G' to be the thermochemical contribution to the Helmholtz energy and add a hyperelastic material with a homogenous strain energy function $A^{\text{el}}(n_i, V)$:

$$A(n_i, V) = G'(n_i) + A^{\text{el}}(n_i, V), \tag{5}$$

which is a homogenous function in n_i and V. Several such functions are available and generally depend on Δ^{el}, expressed in one of the configuration volumes in Fig. 1 [22]. By definition, one has

$$P \equiv -\frac{\partial A}{\partial V} = -\frac{\partial A^{\text{el}}}{\partial V}, \tag{6}$$

and

$$\mu_i \equiv \frac{\delta A}{\delta n_i} = \mu_i' + \frac{\partial A^{\text{el}}}{\partial n_i}, \tag{7}$$

and the Maxwell relation $\frac{\partial \mu_i}{\partial P} = v_i$.

To facilitate discussion in a means useful for small deformations, in this paper, we employ a simplified dilation-only strain energy function expressed in the stress-free configuration:

$$A^{\text{el}} = V^{\text{sf}} \frac{\kappa}{2} \ln^2 \Delta^{\text{el}}, \tag{8}$$

where κ is the isothermal bulk modulus such that

$$P = -\frac{1}{\Delta^{\text{el}}} \kappa \ln \Delta^{\text{el}}. \tag{9}$$

The chemical potential is

$$\begin{aligned} \mu_i &= \mu'_i + P\Delta^{\text{el}} v_i^{\text{sf}} [1 - 0.5 \ln \Delta^{\text{el}}] \\ &= \mu'_i + P v_i [1 - 0.5 \ln \Delta^{\text{el}}], \end{aligned} \tag{10}$$

where $\mu_i'(n_i) \equiv \frac{\partial G'}{\partial n_i}$ is the chemical potential at P^0, and the last line relies on the reasonable assumption that $v_i = \Delta^{\text{el}} v_i^{\text{sf}}$. Equation (10) is a vector equation of v_i^{sf} operating on $P\Delta^{\text{el}}[1 - 0.5 \ln \Delta^{\text{el}}]$. Since $\sum_i v_i^{\text{sf}^2}$ is a scalar and therefore invertible, the Moore-Penrose pseudoinverse may be found, and

$$P = \frac{1}{\Delta^{\text{el}}[1 - 0.5 \ln \Delta^{\text{el}}]} \frac{\sum_i v_i^{\text{sf}} [\mu_i - \mu_i']}{\sum_i v_i^{\text{sf}^2}}, \tag{11}$$

such that the pressure may be related to the change in chemical potential.

For infinitesimal deformations, $\Delta^{\text{el}} \approx 1$, such that $v_i^{\text{sf}} \approx v_i$ and is a constant

$$\mu_i = \mu_i' + P v_i, \tag{12}$$

$$\begin{aligned} P = -\kappa \ln \Delta^{\text{el}} &= \frac{\sum v_i [\mu_i - \mu'_i]}{\sum v_i^2} \\ &\approx \kappa \left[\sum_i c_i v_i^{\text{sf}} - 1 \right], \end{aligned} \tag{13}$$

where the last line is a first-order expansion about the point $\Delta^{\text{el}^{-1}} \to 1$.

C. Expression in the Eulerian frame of reference

Having established the thermodynamic model, we now consider the system in an Eulerian frame of reference discretizing space with a constant volume which for simplicity is taken to be V^0. The Helmholtz energy density $a(c_i, \Delta) = \frac{A}{V^0}$ is thus defined with respect to the reference volume, the dilation, and concentration having been defined above. Since A is homogenous in n_i and V, $A = -PV + \sum \mu_i n_i$, and

$$a = -P\Delta + \sum \mu_i c_i. \tag{14}$$

The Gibbs $g = \frac{G}{V^0}$ and Grand $\psi = \frac{\Psi}{V^0}$ potential densities are likewise defined.

The Helmholtz energy density, therefore, becomes from Eq. (5)

$$\begin{aligned} a &= g'(c_i) + a^{\text{el}}(c_i, \Delta^{\text{el}}) \\ &= \sum c_i \mu'_i + \frac{1}{\Delta^{\text{el}}} \frac{\kappa}{2} \ln^2 \Delta^{\text{el}} \\ &= \sum c_i \mu_i - \frac{\Delta}{\Delta^{\text{el}}} \kappa \ln \Delta^{\text{el}}, \end{aligned} \tag{15}$$

where the last line follows directly from Eq. (14) with Eq. (9) due to homogeneity. In the absence of stress-free dilations, $v_i^0 = v_i^{\text{sf}}$, $\Delta = \Delta^{\text{el}}$, and therefore, $a = \sum c_i \mu_i + \kappa \ln \Delta^{\text{el}}$. Note, in this paper, that the total and elastic dilations depend only on concentrations weighted by their specific volumes, as defined in Eqs. (3) and (4). Therefore, the Helmholtz energy density in the Eulerian frame of reference is only a function of the concentrations in the same frame, $a(c_i, \Delta^{\text{el}}(c_i)) = a(c_i)$.

The Grand potential density may be calculated using Eq. (11):

$$\psi(\mu, \Delta) = -\frac{\Delta}{\Delta^{\text{el}}[1 - 0.5 \ln \Delta^{\text{el}}]} \frac{\sum_i v_i^{\text{sf}} [\mu_i - \mu_i']}{\sum_i v_i^{\text{sf}^2}}. \tag{16}$$

In infinitesimal dilation, $\Delta^{\text{el}} \to 1$ and $\Delta \to 1$ such that $\psi = -\frac{\sum_i v_i [\mu_i - \mu_i']}{\sum_i v_i^2}$.

As an illustration of this approach, consider the following. The model may be nondimensionalized with a natural energy scale $\text{RT}\rho^0$, pressure P^0, and density $\rho^0 = \sum c_i$ at $P = P^0$. Scaled quantities $\tilde{c}_i = \frac{c_i}{\rho^0}$ and $\tilde{P} = \frac{P}{P^0}$ are the scaled concentrations and pressure and are on the order of unity. Equation

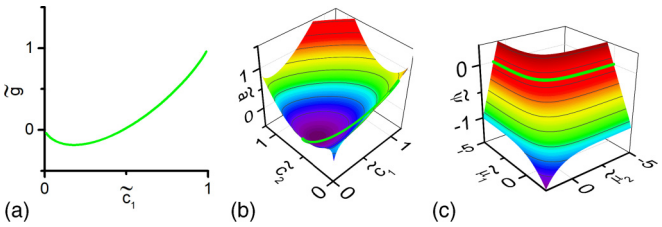

FIG. 2. Demonstrated free energy surface for an ideal binary solution showing the (a) scaled Gibbs energy density at $P = P^0$ as is commonly available in the literature. (b) Scaled Helmholtz and (c) Grand potential densities, derived using the model described above, where the green curve corresponds to $P = P^0$ in (a).

(15) becomes

$$\tilde{a} = \sum \tilde{c}_i \frac{\mu_i}{\mathrm{RT}^0} - \frac{\Delta}{\Delta^{\mathrm{el}}} \tilde{\kappa} \ln \Delta^{\mathrm{el}}, \tag{17}$$

where $\tilde{\kappa} = \frac{\kappa}{\mathrm{RT}\rho^0}$ is a scaled bulk modulus in which, for example, water at room temperature is ~15. The scaled Helmholtz energy is $\tilde{a} = \frac{a}{\mathrm{RT}\rho^0}$, and $\tilde{g}$ and $\tilde{\psi}$ are similarly defined. Further, $\Delta^{\mathrm{el}\,-1} = \sum \tilde{v}_i^{\mathrm{sf}} \tilde{c}_i$, where $\tilde{v}_i^{\mathrm{sf}} = v_i^{\mathrm{sf}} \rho^0$ is the scaled specific volume and is on the order of unity. An illustration of this approach is presented in Fig. 2 with $\tilde{g}(\tilde{c}_1, \tilde{c}_2, \tilde{P} = 1) = \tilde{c}_1[1 + \ln \frac{\tilde{c}_1}{\tilde{c}_1+\tilde{c}_2}] + \tilde{c}_2 \ln \frac{\tilde{c}_2}{\tilde{c}_1+\tilde{c}_2}$, $v_i^{\mathrm{sf}} = \langle 1, 2 \rangle$, and $\tilde{\kappa} = 1$.

Incompressible materials and the lattice constraint

For incompressible materials, $\kappa \to \infty$, $\Delta^{\mathrm{el}} = 1$, and from Eq. (4) becomes an equality constraint $\sum_i c_i v_i = 1$. The pressure may no longer be determined by Eq. (9) but may be determined as the Lagrange multiplier affecting the constraint when forming the multiphase potential, as described below in the context of Eq. (29).

Alternately and commonly, incompressibility is interpreted to be a lattice constraint and is used to eliminate one of the species. In such a case, diffusion of species i implies counterdiffusion of j such that the local volume is unchanged $v_i J_i = -v_j J_j$. Assuming equal mobilities and no spacial variation in specific volume, the interdiffusion potential is

$$\mu_i - \frac{v_j}{v_i}\mu_j = \mu_i' - \frac{v_j}{v_i}\mu_j' + P\left[1 - \frac{v_j}{v_i}\right], \tag{18}$$

and in the case where $v_i = v_j$ simply becomes $\mu_i - \mu_j = \mu_i' - \mu_j'$ regardless of the pressure. This implies that diffusion is not directly affected by the pressure, although the pressure may still play a role in other aspects of system evolution.

D. Linearization of state variable dependences via quadratic potentials

In the ensuing discussion, the ability to invert the functional form of $\mu_i(c_j)$ to find $c_i(\mu_j)$ will be important [10,17,23]. Since $\mu_i(c_j)$ is generally nonlinear, inversion may be facilitated by forming a quadratic potential as a series expansion of the free energy about a known point denoted by an asterisk superscript, from which one linearizes the

$$\mu_i - \mu_i^* = \frac{\partial \mu_i}{\partial c_j}[c_j - c_j^*] \tag{19}$$

relationship [10,17]. It is noted that the approximation as a quadratic potential breaks the homogeneity condition.

The pressure in Eq. (9) may be expanded in terms of $\Delta^{\mathrm{el}\,-1}$ and with Eq. (4) becomes

$$\begin{aligned} P - P^* &= \left[\kappa + \frac{P^*}{\Delta^{\mathrm{el}*}}\right] \sum_i v_i^{\mathrm{sf}}[c_i - c_i^*] \\ &= \left[\kappa + \frac{P^*}{\Delta^{\mathrm{el}*}}\right] \sum_i v_i^{\mathrm{sf}} \frac{\partial \mu_i}{\partial c_j}^{-1}[\mu_j - \mu_j^*], \end{aligned} \tag{20}$$

or if the expansion point is at $P^* = 0$, $P = \kappa \sum_i v_i^{\mathrm{sf}}[c_i - c_i^*] = \kappa \sum_i v_i^{\mathrm{sf}} (\frac{\partial \mu_i}{\partial c_j})^{-1}[\mu_j - \mu_j^*]$. This form is useful, as it defines a linear relationship between unknown variables c_i or μ_i in terms of a known pressure that can be used to impose constraints on the system of interest.

Examining the form of $\frac{\partial \mu_i}{\partial c_j}$,

$$\begin{aligned} \frac{\partial \mu_i}{\partial c_j} &= \frac{\partial \mu'_i}{\partial c_j} + \frac{\partial^2 a^{\mathrm{el}}}{\partial {c_j}^2} \\ &= \frac{\partial \mu'_i}{\partial c_j} + v_i \frac{\partial P}{\partial c_j} \\ &= \frac{\partial \mu'_i}{\partial c_j} + \frac{\kappa}{\sum c_i v_i^0} v_i^0 v_j^0 \,[1 - \ln \Delta^{\mathrm{el}}], \end{aligned} \tag{21}$$

where we have first used the Maxwell relation $\frac{\partial \mu_i}{\partial P} = v_i$. For infinitesimal displacement, this becomes

$$\frac{\partial \mu_i}{\partial c_j} - \frac{\partial \mu'_i}{\partial c_j} = \kappa v_i v_j. \tag{22}$$

The introduction of the elastic energy thus changes the linearization by terms related to the specific volumes and the bulk modulus. The case of interdiffusion, i.e., a constant volume, Eq. (22) implies an increase in local pressure which would be dissipated via diffusion and the applied boundary conditions.

The matrix $\frac{\partial \mu_i}{\partial c_j} = \frac{\partial^2 a}{\partial c_i \partial c_j}$ is necessarily symmetric, and similarly for $\frac{\partial \mu'_i}{\partial c_j} = \frac{\partial^2 a'}{\partial c_i \partial c_j}$. However, since a' is a first-order homogenous function in c_i, $\frac{\partial \mu'_i}{\partial c_j}$ has rank $k - 1$ due to the Gibbs-Duhem relation and is therefore singular. This singularity is resolved through the application of the lattice constraint which breaks the homogeneity of the potential, e.g., ideal mixing where $\mu'_i = \mu_i^0 + \mathrm{RT} \ln \frac{c_i}{\sum c_j}$, imposition of a dilute approximation or the lattice constraint breaks the homogeneity of the function through removal of the term $\sum_i c_i$. In contrast, in this paper, $\frac{\partial \mu_i}{\partial c_j}$ is not in general singular since the differentiation is not with respect to all extrinsic variables due to the introduction of Δ [17]. In Eq. (21), this dependence is captured by the second term which is symmetric, positive semidefinite, and rank 1. The addition of this term makes $\frac{\partial \mu_i}{\partial c_j}$ full rank and invertible either through numerical or analytical means [17].

III. MULTIPHASE COMPOSITE POTENTIAL

We now expand the single-phase model above to a multiphase material. In the ensuing derivation, properties are phase independent unless indexed by a superscript Greek letter.

Consider a multiphase material that is undergoing a phase change. The extent of the phase change may be parameterized by the extrinsic quantity $V^0 p^\pi$, where p^π is the dimensionless volume fraction of the material in phase π and varies from 0 to 1. This parameterization may be envisaged as an element with a sharp interface that is progressing or a homogenous material in a superposition of pure phase states. The corresponding fundamental equation is [24]

$$\begin{aligned} dU &= -PdV + \sum \mu_i dn_i - \sum B^\pi d(V^0 p^\pi) \\ du &= -Pd\Delta + \sum \mu_i dc_i - \sum B^\pi dp^\pi, \end{aligned} \tag{23}$$

which defines the driving force for the phase change in terms of the characteristic thermodynamic potentials:

$$-B^\pi \equiv \left.\frac{\partial a}{\partial p^\pi}\right|_{\Delta, c_i} = \left.\frac{\partial \psi}{\partial p^\pi}\right|_{\Delta, \mu_i}. \tag{24}$$

We further assume the local equilibrium approximation, i.e., the relaxation of internal degrees of freedom of coexisting phases at the interface to a local equilibrium such that $\mu_i^\pi = \mu_i$, and the equilibrium partitioning of n_i^π in their respective phases [24]. Equivalence of μ_i in coexisting phases implies a multiphase composite potential may be defined in terms of the sum of single-phase Grand potentials weighted by the phase parameterization:

$$\psi(\mu_i, \Delta^\pi, p^\pi) = \sum_\pi \psi^\pi(\mu_i, \Delta^\pi) p^\pi. \tag{25}$$

This formulation is popular in phase-field literature, as it has been shown to decouple states of coexisting bulk phases from the interface such that no implicit contributions to interfacial energy occur [10,20,25]. Since $\frac{\partial \psi}{\partial \mu_i} = -c_i$, the phase-specific concentrations follow the intuitive relation:

$$\sum_\pi c_i^\pi p^\pi = c_i. \tag{26}$$

It is at this point that this approach differentiates itself. Since the definition of the phase parameterization $V^0 p^\pi$ involves volume change of phase π, we cannot specify (or expect in general) P^π to be equal. Rather, the equilibrium between the variation of the phase volumes defines the discontinuous value of P^π [26]. This pressure is a new degree of freedom in this approach which needs not to be explicitly calculated but rather emerges from the requirement that all μ_i^π are equal. This formulation then naturally permits the model to account for pressure/dilation variation between phases which affords the freedom to capture curvature and kinetic effects.

The Grand potential density of each phase is

$$\begin{aligned} \psi^\pi &= a^\pi - \sum_i \mu_i c_i^\pi \\ &= -\Delta^\pi P^\pi. \end{aligned} \tag{27}$$

In this paper, ψ^π is readily expressed through Eq. (28), through Eq. (3), and with pressure from Eq. (9) or with a Lagrange multiplier as discussed below. Other models rely on Eq. (27), as discussed in the model formulations section below [10].

A. Incompressible materials and connection to the lattice constraint

We now briefly return to the calculation of pressure in the incompressible case. Equation (25) implies a minimization which including the incompressibility constraint reads [19]

$$\begin{aligned} a(c_i, \Delta^\pi, p^\pi) = \min \sum_\pi a^\pi(c_i^\pi, \Delta^\pi) p^\pi \\ \text{subject to} \quad \begin{matrix} \sum_\pi c_i^\pi p^\pi = c_i \\ \sum_i v_i^{\mathrm{sf}\pi} c_i^\pi = \Delta^\pi \end{matrix}. \end{aligned} \tag{29}$$

Forming the Lagrangian $\mathcal{L} = \sum_\pi a^\pi(c_i^\pi, \Delta^\pi) p^\pi + \sum \mu_i [c_i - \sum c_i^\pi p^\pi] - P^\pi [\Delta^\pi - v_i^{\mathrm{sf}\pi} c_i^\pi]$, where the Lagrange multipliers are identified as the dual variables of the parameter in the constraint. This is most easily seen via the envelope theorem $\frac{\partial a}{\partial \Delta^\pi} = \frac{\partial \mathcal{L}}{\partial \Delta^\pi} = -P^\pi$ and likewise for μ_i. Therefore, the pressure in each phase may be calculated uniquely in the incompressible case while forming the composite potential.

B. Governing equations

The governing equations may be derived from the theory of irreversible processes, sometimes referred to as nonequilibrium thermodynamics, to generate entropy locally [27]. Mass transport in each phase is given as

$$\dot{c}_i^\pi = -\nabla \cdot J_i^\pi + Q_i^\pi, \tag{30}$$

where Q_i^π is the volumetric mass sources/sinks. The mass fluxes are derived from linear phenomenological theory assuming no interdiffusion cross-terms $J_i^\pi = -c_i^\pi M_i^\pi \nabla \mu_i$ [28,29], where M_i^π is the mobility coefficient. Notably, the definition of the mass flux permits $M_i^\pi \neq M_j^\pi$ in general. Equation (30) is useful to implement in sharp interface models which consider phases as separate computational domains [16]. Alternately, the total rate of change of c_i, useful in phase-field models, can be expressed via Eq. (26):

$$\begin{aligned} \dot{c}_i &= -\nabla \cdot \sum_\pi p^\pi J_i^\pi + \sum_\pi p^\pi Q_i^\pi \\ &= -\nabla \cdot \left[\sum_\pi p^\pi c_i^\pi M_i^\pi \right] \nabla \mu_i + \sum_\pi p^\pi Q_i^\pi, \end{aligned} \tag{31}$$

or if the diffusivity of species is equal in all phases, $M_i = M_i^\pi$:

$$\dot{c}_i = -\nabla \cdot c_i M \nabla \mu_i + \sum_\pi p^\pi Q_i^\pi. \tag{32}$$

The local state of composition and evolution via Eq. (32) may be described by either variable of the μ_i-c_i conjugate pair. The chemical potential benefits from being constant across an interface in equilibrium, whereas the concentration typically varies either in relative composition or density between equilibrium states, requiring suitable numerical discretization.

However, material properties are often expressed as nonlinear functions of nominally extrinsic variables, e.g., $\mu_i(c_j)$.

The rate of phase change depends on the method of representing phase but is proportional to B^π, with proportionality constant M_ϕ, which may be related to interface attachment kinetics [17]. When interfacial effects are relevant or in phase-field models, an interfacial energy term f_{int} is included which contributes to the phase change [30]:

$$\dot{p} = M_\phi \left[B^\pi + \frac{\partial f_{\text{int}}}{\partial p} \right]. \tag{33}$$

The expression of B^π via Eq. (24) corresponds to the potential for which the choice of state variables representing composition are the natural variables. Thus, $B^\pi = -\frac{\delta\psi}{\delta p^\pi}|_{\mu_i}$ or $B^\pi = -\frac{\delta a}{\delta p^\pi}|_{c_i}$ for the choice of μ_i [10,23] or c_i [17,21], respectively.

IV. COMPARISON OF MODELS

To compare the implications of the current model with models which invoke the lattice constraint, we consider a set of four models probing quadratic approximations and diffuse vs sharp interface models. These models are applied to the well-established case of a spherical nanoparticle to show recovery of classical theory followed by free dendritic growth to elucidate the importance of this paper in future research on microstructure growth.

To explore the implications of this paper on simulation results, four models are compared using the sharp and diffuse interface representations with choices for c_i or μ_i as dynamic variables, identified as A–D:

A. Sharp interface in c_i, implementing the current approach with an exact potential;

B. Phase-field in μ_i, implementing the current approach with a quadratic potential;

C. Phase-field in μ_i, implementing the lattice constraint with a quadratic potential; and

D. Phase-field in μ_i, implementing the lattice constraint with an exact potential.

All models were solved in one dimension (1D) using the finite element method. Model A was implemented in COMSOL Multiphysics v5.5 [31]. Models B–D were implemented in the FENICS package [32–35]. Since this model formulation requires an additional field variable as compared with the lattice constraint, the computational burden increases accordingly. For a binary scenario, this implies doubling the vector of unknowns and the dimensions of the (sparse) Jacobian. For these cases, a direct solver was used which nominally would imply an increase in computational complexity/wall time of a maximum factor of 8. In practice, however, the additional computational cost was observed to be significantly less which implies the solution of the Newton step was not the rate-controlling step. For increasingly multicomponent systems, this incremental burden decreases.

In preliminary investigations of iterative methods for the solution of the Newton step, it was also noted that models in the current formulation appear stiffer. This is likely due to the relative magnitude of the elastic response as compared with the chemical response, e.g., the factor of bulk modulus appearing in the pressure and its effect on μ_i per Eq. (21). This implies an eigenvector of the Jacobian in the vector $\langle v_i c_i \rangle$ and that a suitable preconditioner should be employed. The efficient implementation of this method is left for subsequent work.

A. Model A: Sharp interface approach with this paper

The sharp interface model consisted of two 1D domains on a moving mesh with a shared boundary. Each domain represents a phase in which c_i is the dynamic variable, and $\mu_i = \frac{\partial a}{\partial c_i}$. The shared boundary represents the phase boundary at which $J_i^s = J_i^l$, and local equilibrium $\mu_i^l = \mu_i^s$ is applied via a Lagrange multiplier. Note this is a generalization of the Stefan model, as will be discussed elsewhere. The position z_{int} of the interface can be related to the phase fraction p. The velocity of the interface corresponds to the rate of phase change in Eq. (33), and since the chemical potential is held constant, $B^\pi = -\frac{\partial\psi}{\partial p}$. The interfacial energy is $f_{\text{int}} = \sigma\, 4\pi z_{\text{int}}^2$, and therefore,

$$\dot{z}_{\text{int}} = \dot{p} = M_\phi \left[\psi^l - \psi^s - \frac{2\sigma}{r} \right], \tag{34}$$

with pressure calculated by Eq. (9):

$$\psi^\pi = \sum_i c_i^\pi \cdot \kappa^\pi \ln \sum_i c_i^\pi. \tag{35}$$

A constraint of $P^l = 0$ is applied at the outer boundary as a Dirichlet condition.

For phase-field models, a phase-indicator ϕ is introduced as the arguments to $p(\phi)$ and $f_{\text{int}}(\phi, \nabla\phi)$. The governing equations become

$$\begin{aligned} \dot{\phi} &= B^\pi \frac{\partial p^\pi}{\partial \phi^\pi} + \frac{\delta f_{\text{int}}}{\delta \phi} \\ &= [\psi^s - \psi^l] \frac{\partial p}{\partial \phi} - \sigma \left[6d\nabla^2\phi - \frac{3}{d} \frac{\partial \phi^2 [1-\phi]^2}{\partial \phi} \right]. \end{aligned} \tag{36}$$

The mass transport is assumed to be quasistatic with equal mobilities, however, and therefore, from Eq. (32):

$$\begin{aligned} \dot{c} &= \nabla \cdot c_i M_i \nabla \mu_j, \\ \dot{\mu}_i \frac{\partial c_j}{\partial \mu_i} + \dot{\phi} \frac{\partial c_j}{\partial \phi} &= \nabla \cdot c_i M_i \nabla \mu_j, \\ \dot{\phi} \frac{\partial c_j}{\partial \phi} &= \nabla \cdot c_i M_i \nabla \mu_j. \end{aligned} \tag{37}$$

B. Model B: Phase-field model with this paper and quadratic potential

Expanding a quadratic about a point c_i^*, $f - f^0 = \frac{1}{2}\sum [c_i - c_i^*][\mu_i + \mu_i^0]$, where the relationship between μ_i and c_i is via Eq. (20) with $P^l = 0$, and Grand potential via Eq. (28):

$$\psi - \psi^* = -\kappa \sum_i \frac{\partial c_i}{\partial \mu_j} [\mu_j - \mu_j^*]. \tag{38}$$

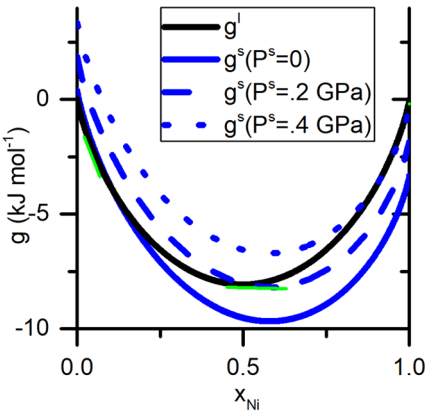

FIG. 3. Displacement of Gibbs free energy curves by P^s with $v_i = 1$. The tie line indicating equilibrium is shown in green for the three equilibria.

C. Model C: Phase-field model with lattice constraint and quadratic potential

Like Model B, the quadratic lattice approach uses the relationship between μ_i and c_i given in Eq. (19). The Grand potential can then be found by similarly expanding Eq. (27):

$$\psi - \psi^* = -\frac{1}{2}\sum_i [\mu_i - \mu_i^*][c_i + c_i^*], \tag{39}$$

for both phases. Since the lattice constraint is assumed, this model only considers a single species.

D. Model D: Phase-field model with lattice constraint and an analytical potential

The ideal case takes advantage of the invertible form of an ideal binary solution. Considering an ideal binary solution, $f = c[a + \ln c] + [1 - c][b + \ln(1 - c)]$, one calculates $\mu = \frac{\partial f}{\partial c} = (a - b) + \ln\frac{c}{1-c}$, which may be inverted analytically to find $c(\mu) = [1 + \exp(a - b - \mu)]^{-1}$. The Grand potential is then calculated by Eq. (27):

$$\begin{aligned}\psi &= f - \mu c \\ &= b + \ln(1 - c) \\ &= b + \ln\left(1 - \frac{1}{1 + \exp(a - b - \mu)}\right).\end{aligned} \tag{40}$$

The free energies used in this demonstration correspond to the Ni-Cu system given by

$$g'^s(c_{\mathrm{Ni}},\ c_{\mathrm{Cu}}) = x_{\mathrm{Ni}}L_{\mathrm{Ni}}\frac{T - T^m_{\mathrm{Ni}}}{T^m_{\mathrm{Ni}}} + x^s_{\mathrm{Cu}}L_{\mathrm{Cu}}\frac{T - T^m_{\mathrm{Cu}}}{T^m_{\mathrm{Cu}}} + \frac{\mathrm{RT}}{v_m}[x_{\mathrm{Ni}}\ln x_{\mathrm{Ni}} + x_{\mathrm{Cu}}\ln x_{\mathrm{Cu}}], \tag{41}$$

$$g'^l(c_{\mathrm{Ni}},\ c_{\mathrm{Cu}}) = \frac{\mathrm{RT}}{v_m}[x_{\mathrm{Ni}}\ln x_{\mathrm{Ni}} + x_{\mathrm{Cu}}\ln x_{\mathrm{Cu}}], \tag{42}$$

with the mole fractions $x_{\mathrm{Ni}} = \frac{c_{\mathrm{Ni}}}{c_{\mathrm{Ni}}+c_{\mathrm{Cu}}}$ and $x_{\mathrm{Cu}} = \frac{c_{\mathrm{Cu}}}{c_{\mathrm{Ni}}+c_{\mathrm{Cu}}}$ and properties listed in Table I.

The equilibrium at $T = 1400$ K and $P^l = 0$ (GPa) is depicted as tie lines in the Gibbs free energy plot in Fig. 3,

TABLE I. Parameters for the Ni-Cu system demonstrative model from Refs. [9,37,38]. Bulk moduli, κ^π and the interfacial energy σ are representative. The specific volumes are at 1400 K, and v_m is the assumed average specific volume for cases neglecting density variation.

Symbol	Value	Unit
T^m_{Ni}	1728	K
T^m_{Cu}	1358	K
L_{Ni}	2350	J cm^{-3}
L_{Cu}	1748	J cm^{-3}
σ	1.0	J m^{-2}
κ^s	100	GPa
κ^l	1	GPa
v_m	7.42	cm^3 mol^{-1}
v^s_{Ni}	6.99	cm^3 mol^{-1}
v^l_{Ni}	7.29	cm^3 mol^{-1}
v^s_{Cu}	7.72	cm^3 mol^{-1}
v^l_{Cu}	8.12	cm^3 mol^{-1}

wherein the energy of the solid phase is raised vertically by P^s since specific volumes of species are assumed equal. The tie lines are determined through the equilibrium partitioning x^{s*}_{Ni} and x^{l*}_{Ni}, requiring $\mu^s_i(x^{s*}_{\mathrm{Ni}}) = \mu^l_i(x^{l*}_{\mathrm{Ni}})$, or equivalently the geometric lowest common tangent approach:

$$\begin{aligned}&\frac{\partial g^s}{\partial x_{\mathrm{Ni}}}(x^{s*}_{\mathrm{Ni}}) = \frac{\partial g^l}{\partial x_{\mathrm{Ni}}}(x^{l*}_{\mathrm{Ni}}), \\ &g^s(x^{s*}_{\mathrm{Ni}}) + P^s = g^l(x^{l*}_{\mathrm{Ni}}) + [x^s_{\mathrm{Ni}} - x^{l*}_{\mathrm{Ni}}]\frac{\partial g^l}{\partial x_{\mathrm{Ni}}}(x^{l*}_{\mathrm{Ni}}).\end{aligned} \tag{43}$$

The maximal pressure attainable is calculated as $\Delta P^{\max} = g^s(x_{\mathrm{Ni}} \to 1) - g^l(x_{\mathrm{Ni}} \to 1) = L_{\mathrm{Cu}}\frac{T - T^m_{\mathrm{Cu}}}{T^m_{\mathrm{Cu}}} = 0.446$ GPa.

E. Spherical nanoparticle equilibria

We first consider the equilibrium of a solid nanoparticle with radius r in a liquid. Equilibrium is described by the classical Young-Laplace relation:

$$P^s_r - P^l = \frac{2\sigma}{r}, \tag{44}$$

such that, as $r \to \infty$, the flat interface is approached with $P^s = P^l$, which represents bulk equilibrium. The chemical potentials at equilibrium are constant throughout the system but are shifted by the pressure in the enclosed phase and compositional change. It will be demonstrated that, while both formulations produce Eq. (44), the extra degree of freedom afforded by this paper allows for explicit control of P^l, which may be relevant to experimental conditions and necessary for future inclusion of structural mechanics/fluid flow. Equation (44) implies a critical radius of 4.484 nm in the construction of Fig. 3 as the smallest embryo which can be stable with the melt.

A simple classical solution occurs when the composition of the solid phase does not vary, possibly due to high curvature in the energy potential approaching the stoichiometric case. If v^s_i is not a strong function of pressure (therefore, $\Delta^{\mathrm{el}} \to 1$)

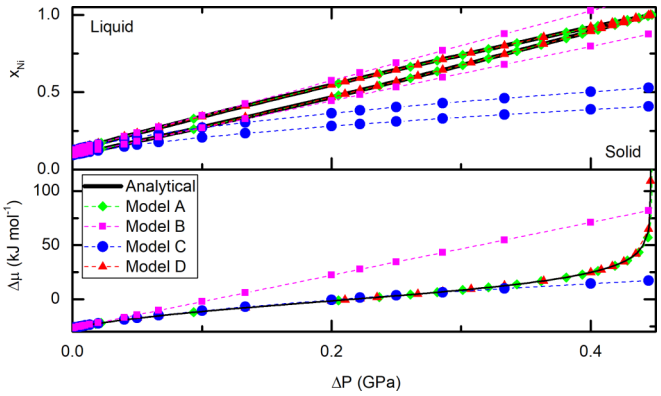

FIG. 4. Simulation results of mole fraction (above) and interdiffusion potential (below) at the interface, plotted along with the Young-Laplace equations. The solid line represents the analytical solution; models A and B are implementations of this paper, and models C and D implement the lattice constraint.

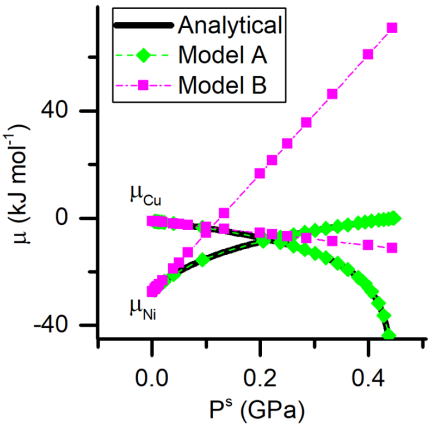

FIG. 5. Comparison of the chemical potentials of species 1 (solid line) and 2 (broken line) for models A and B based on this paper, showing the effect of linearization vs the sharp interface implementation.

[26],

$$\mu_{ir} - \mu_{i\infty} \approx v_i^s \frac{2\sigma}{r}. \tag{45}$$

In this approach, Eq. (18) readily shows that, for equal specific volumes, pressure does not require a compositional change since the pressure is reflected either by the Lagrange multiplier or a change in Δ^{el} corresponding to all species being multiplied by a factor $c^s_{i,r} = c^s_{i,\infty} \exp(\frac{P^s_r - P^s_\infty}{\kappa^\beta})$. Equation (45) is then recovered directly from Eq. (10) when $\Delta^{\mathrm{el}} \to 1$ since μ_i' only depends on the relative concentrations. The term $1 - \frac{1}{2}\ln\Delta^{\mathrm{el}}$,- which depends on the form of the pressure in Eq. (9), can therefore be seen to modify this relation in the general case of compressible materials. Since the pressure of the surrounding liquid remains at P^l_r, the chemical potential variation is accommodated by a change in relative compositions.

The general case of a two-component system with compositions in which both phases can vary is investigated with models A–D. To aid in comparison, dilation is infinitesimal, all $v_i^{0^\pi} = 1$, and we are only concerned with stationary, i.e., equilibrium solutions with $\dot{c}_i = 0$. This approach affords the degree of freedom to fix $p^l = 0$ at the outer boundary which is done where possible. The case is contrived to correspond to the discussion in Refs. [24,36].

The equilibrium mole fractions in the solid and liquid phases and interdiffusion potential are plotted in Fig. 4 along with the simulation results. Analytics results are obtained through iterative methods to solve Eq. (43) in the same manner as to determine tie lines in Fig. 3.

Figure 4(a) shows that models A and D both follow the analytical calculations of solubility well as the logarithmic behavior of the potential, and therefore $\mu_i(c_i)$ is preserved. Both quadratic models B and C show roughly linear trends after a slight curvature in the lattice model at small ΔP. Model B, however, brackets the analytical result, while C underpredicts the solubility curve as pressure increases. Models B and C also differ in the magnitude of the partitioning $c_i^l - c_i^s$.

Models A and D predict $\Delta\mu_i$ accurately for a large range of pressures, again due to their capturing of the logarithmic dependence which models B and C disregard. Models B and C produce linear trends, as expected by Eq. (15); however, here, the impact of this approach is noted via Eq. (22) which causes the trends to separate. Figure 5 shows how Model B follows a linear approximation of $\mu_i(\Delta P)$ at $\Delta P = 0$ which deviates from the analytical solution rapidly.

The predicted pressures are shown in Fig. 6. Models A and B can be seen to maintain $P^l = 0$ using the degree of freedom afforded by the current approach, while models C and D overpredict the pressures in both phases. Nonetheless, all simulations show good agreement between $\Delta P(r)$ and Eq. (44).

Densification is also predicted in models A and B and shown in Fig. 7. The concentrations of species in the solid phase shown in Fig. 7 (above) are the combined dependence

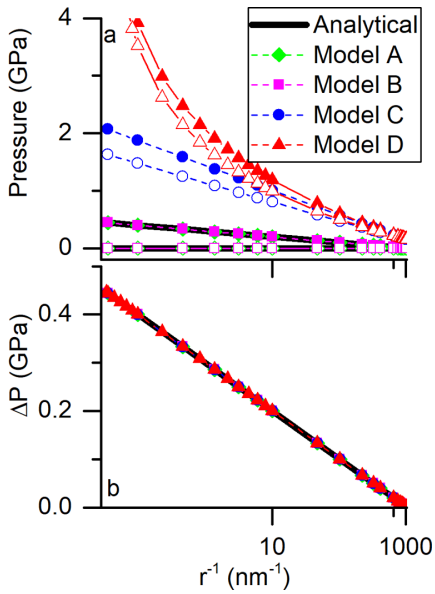

FIG. 6. Predicted pressures as a function of radius. Open and closed symbols above correspond to liquid and solid phases, respectively.

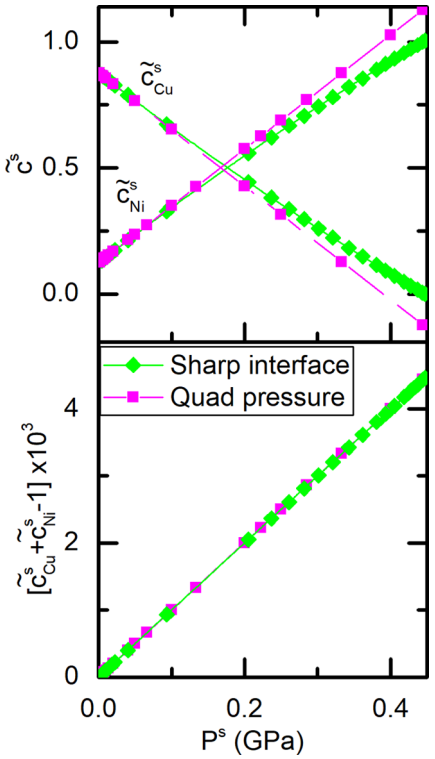

FIG. 7. Solid-phase concentrations with P^s predicted from the sharp interface and quadratic pressure models. The top plot shows the individual species concentrations scaled by v_m, showing $\tilde{c}^s_{Cu} < 0$ at high pressure, which is permissible in the quadratic expansion but prevented in the sharp interface by the asymptotic behavior of μ_i. The bottom plot shows the total concentration in the solid phase which exceeds 1, reflecting elastic compression linearly related to the pressure. Since κ^s is large, $\sum c_i^s \approx 1$, and therefore, $\Delta^{el} \approx 1$, which justifies the linear expansion in Eq (20).

of the shift in solubility with P^s and densification of the solid phase. Densification of the solid phase is more clearly seen in Fig. 7 (below) which shows the total concentration in the solid phase as it increases with P^s approximately linearly as per Eq. (13) due to infinitesimal dilation.

Figure 6 shows that all four models accurately reproduce the dependence of the relative pressure on particle radius described in Eq. (44), which is expected as the equilibrium of the phase evolution Eq. (33). Likewise, the balance of chemical potentials/interdiffusion potentials is assured by Eq. (30) and their dependence on the relative pressure governed by the construction shown in Fig. 3. Thus, the good agreement between simulation and analytical results shown for all models in Fig. 4 is anticipated. The difference between this approach and lattice-constrained models, therefore, falls on the interpretation of the pressure and its calculation via Eqs. (35) and (38)–(40) for the sharp interface, ideal lattice, quadratic lattice, and quadratic pressure, respectively.

This approach introduces an elastic term to form the Helmholtz free energy in Eq. (5). Since $A(n_i, V)$ is homogenous in n_i and V, one is assured that $A(n_i, V) = \sum_i n_i\mu_i - PV$ with the conjugate variables defined in Eqs. (9) and (10) from which the Grand potential is $\Psi = A - \sum_i n_i\mu_i = -PV$. The equivalence between the Grand potential and the pressure defined in Eq. (9) therefore relies on the homogeneity of the free energy, which is broken by the assumption of the lattice constraint or approximation with a quadratic potential. More precisely, the difference is the inhomogeneity of the free energy which implicitly contributes to Ψ. For this reason, the quadratic expansion of the current model relies on the linearization of P in Eq. (20). The result is a good approximation of the solubility change in Fig. 4 (top) by the quadratic expansion of this approach. Auxiliary calculations relying instead on Eq. (9) for the driving force showed equivalent predictions to the quadratic lattice case.

When one approximates the potentials with quadratic expansions, it is expected that the equilibrium composition and potentials be modified, as seen in Fig. 4 in both cases. The apparently poor prediction of interdiffusion potential by the quadratic pressure model is shown to be a consequence of the linearization of μ_{Ni} and μ_{Cu} individually in Fig. 5, whereas the quadratic lattice model expands $\mu_{Ni} - \mu_{Cu}$ directly.

F. Free dendritic growth

The demonstrations we have presented thus far have shown the quantitativeness of our model formulation in exhibiting pressure and density variations. These were performed, for convenience, under the constraint all $v_i^0 = 1$. However, real materials have variable specific volumes across species and phases. To further highlight the capabilities of the model, we now demonstrate it for free dendrite growth using Model B. Note this paper excludes shear strains/stresses which are clearly present in crystalline systems such as this, and bulk motion in the liquid phase is also ignored as a simplification. However, the application of this model to free dendritic growth serves to highlight the importance of variable specific volume and is therefore nonetheless informative.

For this demonstration, we contrast our model under conditions where we impose the constraint that all $v_i^0 = 1$ with that where we utilize realistic phase-specific volumes which vary between species and phase listed in Table I. We additionally set $M_l = 10^{-8}/\mathrm{RT\,m^2\,s^{-1}}$ as representative [39] and the phase-field interface width $d = 10$ nm. Together with the interfacial energy, these collectively set the energy scale, time scale, and length scale of the problem. For spatial discretization, these simulations are performed using an adaptive mesh refinement algorithm, where the smallest element size is set to $\Delta x = 0.4\ d$. A heuristic adaptive time stepper, based on the number of Newton iterations needed for the solution to converge in a given timestep, is used such that $10^{-3}\tau_0 \leqslant \Delta t \leqslant 10\tau_0$, where $\tau_0 = \frac{d^2}{D_l}$.

Simulations are compared in terms of the applied driving force for phase change. This is controlled in the model through supersaturation:

$$\Omega = \frac{c_i^{\mathrm{avg}} - c_i^{l*}}{c_i^{s*} - c_i^{l*}}, \tag{46}$$

which determines the average concentration c_i^{avg} with $c_i^{\pi *}$ as the bulk equilibrium for $T = 1400$ K. Zero-flux conditions are implemented on all boundaries to maintain the supersaturation. The domain is initialized with a circular solid seed of radius $r = 200$ nm, with composition c_i^{s*} and the liquid with

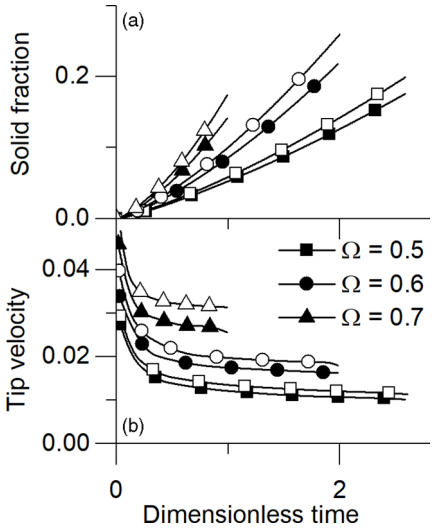

FIG. 8. Comparison of (a) solidification fraction and (b) dendrite tip velocity for three supersaturations vs dimensionless time. Data series are truncated when the tip velocity departs from the steady-state regime. Note that filled symbols showcase simulations where the constraint $v_i^\pi = 1$, and empty symbols correspond to Model B with the specific volumes listed in Table I.

composition c_i^{avg}. Note that this approach does not guarantee $P_l = 0$ due to $c_i^{l*} \neq c_i^{\text{avg}}$ in general and particularly in the case below.

We include anisotropy in the standard fashion by including an order parameter dependence in the surface energy gradient term [40]. Simulations are performed in two dimensions, where a quarter of the growing crystal is simulated due to the cubic fourfold symmetry. We restrict our analysis to the initial transient after initialization and the free growth steady-state regime of the equiaxed single dendritic growth.

The change in solid fraction and dendrite tip velocity vs time are the two measures we use to examine the growth rate. The solid fraction is calculated by integrating the order parameter over the domain. The tip velocity is calculated by determining the interface position through order parameter contour, i.e., $\phi = 0.5$, as a function of time, fitting the result to a cubic spline, and taking the derivative. Both measures are presented in Fig. 8 for different supersaturations. The top panel in the figure displays the solid fraction, where filled symbols represent the simulations with $v_i^\pi = 1$, while the empty symbols represent variable specific volumes according to Table I. It is expected that larger supersaturation would correlate with faster growth rates; however, we also observe faster rates for the case of variable volumes. The bottom panel shows the tip velocity, where we observe results consistent with the solid fraction data, faster steady-state velocities for increasing supersaturation, but also the case of variable specific volume. The possible reasons leading to this behavior when using variable-specific volumes can be attributed to the change in volume affecting the driving force, altering the shape of the growing crystal, or a combination of both. To get a better understanding, we examine the crystal shape and microsegregation next.

To examine the effect of variable specific volumes on dendrite shape, we examine snapshots in three stages of growth for each supersaturation and each set of specific volumes imposed. The results are presented in Fig. 9, where the interface contours are plotted. For each supersaturation, we compare the same time for each volume constraint, while across supersaturations, we have attempted to extract representative cases of early time, i.e., when the crystal begins to assume some anisotropy, intermediate time, when the primary dendrite arms start to establish themselves, and late time, when the crystal has reached the end of the steady-state regime. What is interesting here is the clear differences in the shapes of the growing crystal. Specifically, in the cases of variable volume, the dendrite arms appear thicker and broader for the same time and have progressed further along the primary axes. Other interesting features can be found in the grooves of the primary arms which also exhibit differences as a function of volume such that higher curvature appears with the variable volume case. The structure of the grooves, like the growing tip, is a function of solute segregation, which we consider next.

Solute rejection at the growing interface not only maintains interfacial equilibrium but helps determine the final dendrite shape. In the present formulation, we can also determine the dilation in the phases caused by density variations and the resultant pressure. According to Eq. (13), elastic dilatation can be determined by considering the term $\sum v_i^\pi c_i^\pi - 1$, where the phase is in elastic compression (tension) when the resultant sum is positive (negative). As a demonstrative showcase of the segregation dilation and pressure behavior, we show only a single supersaturation $\Omega = 0.5$ in Fig. 10. The top panel displays segregation, where we observe an initial spike of solute due to the adjustment of the system to the initial capillary pressure increasing local density and redistributing solute per the logic behind Eq. (45). There appears to be a slightly lower concentration in the solid for the case of variable volume for all time, while in the intermediate regime where the crystal has reached steady state, we find that the variable volume case has rejected more solute in the liquid ahead of the front, a quantitative indication of the differing behavior.

When we examine the dilation and pressure in Fig. 10, we note that the choice of controlling Ω and the consequent initial conditions discussed above have created a positive pressure in the liquid. In the early stage of growth, we notice a similar behavior of the initial adjustment leading to a spike in density followed by a tapering off in the solid. This is because the solid is denser than the liquid, creating negative pressure as the solid grows into the liquid. What is notable is that, even though the segregation showed only slight differences, those differences are clear and amplified in the dilation and pressure metrics.

Pressure gradients that appear in Fig. 10 nominally would dissipate through elastic and/or plastic deformation or fluid flow; however, such bulk motion is not included in this paper. Pressure gradients in Fig. 10 in the solid would likely dissipate and equilibrate to a degree via elastic deformation. The dissipation in the liquid is less clear, however, as viscous flow through the dendrite branches would have to occur.

We now discuss the driving force change upon consideration of variable specific volumes. In permitting

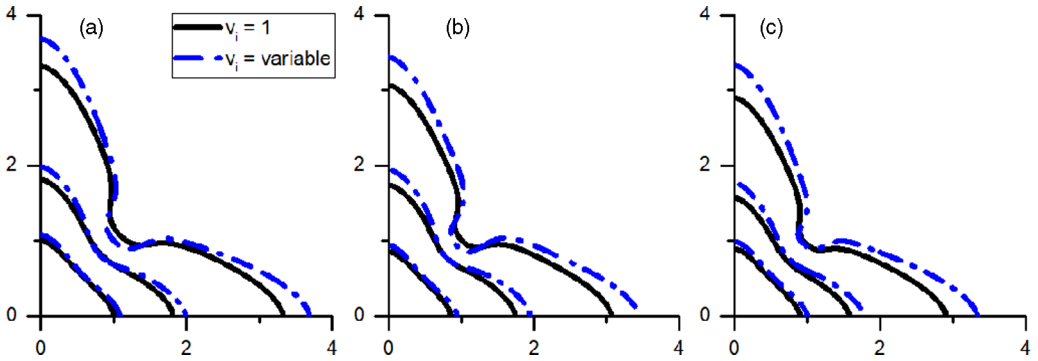

FIG. 9. Interface contour plots for each supersaturation. (a) $\Omega = 0.5$, (b) $\Omega = 0.6$, and (c) $\Omega = 0.7$. In each grid, contours are plotted showing early, mid, and late stages of the free growth regime for the $v_i^0 = 1$ and variable volume cases shown in solid and dash-dot lines, respectively.

pressure/density change, one must consider the tie line for equilibrium between phases to be a tangent surface in $c_{\mathrm{Cu,\ Ni}}$ spanned by the set of possible tie lines. The shape of this surface is affected by the specific volumes, although one would expect from Eq (10) that, for $P^s = P^l = 0$, one would find the same mole fractions which also correspond to the lattice constrained case. The zero pressure equilibrium concentrations are $c^s_{\mathrm{Ni,\ Cu}} = 0.122825,\ 0.877175$ and $c^l_{\mathrm{Ni,\ Cu}} = 0.092425,\ 0.907575$ for the case of $v_i^\pi = 1$ and $c^s_{\mathrm{Ni,\ Cu}} = 0.119404,\ 0.852744$ and $c^l_{\mathrm{Ni,\ Cu}} = 0.0853511,\ 0.838109$ for the variable volume case. Note that the mole fractions are equivalent. This is an indication that the tangent surface that determines the equilibrium solutions for the respective system has also changed. For the same simulation conditions then, we have each system effectively operating in two different phase spaces, as dictated by the tangent surface, that contribute to their kinetic path during growth. The evidence we have presented above then necessarily translates to an increase of the driving force of the variable volume case because of the difference in tie lines and curvatures of the free energies. This can also conversely be interpreted as a change in effective pressure.

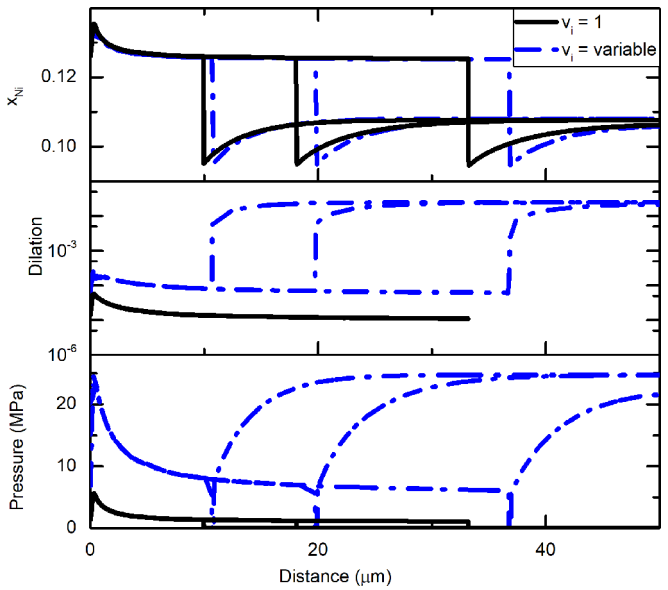

FIG. 10. Mole fraction, dilation, and pressure profiles along the primary lobe for $\Omega = 0.05$, showing early, intermediate, and late stages of the free growth regime for the $v_i^0 = 1$ and variable volume cases shown in solid and dash-dot lines, respectively. Time progresses as the profiles shift to the right.

Inclusion of the variable volumes also affects the dependence of the driving force and local chemical potential on local curvature, as made explicit in Eq. (45) to a first approximation. This contributes to the change in dendrite shape shown in Fig. 9.

It is abundantly clear that the change in specific volume is a factor in determining the shape, segregation, and pressure of the solidifying crystal. Solidification is the initial stage for most industrial materials, particularly with recent technologies such as additive manufacturing and other near-net-shape manufacturing technologies. The results we have presented in this section, though we have not accounted for all phenomena, suggest that to adequately predict the microstructures of these initial system requires model formulations that consider density variations.

As a final note, we remark on the conditions used in this section. In designing the conditions for dendritic growth, we opted here to use the supersaturation as a measure of our driving force and implemented zero-flux boundary conditions accordingly and not according to the Gibbs formulation shown in Fig. 3. However, we note that these conditions lead to an initial liquid state that is pressurized (see bottom panel Fig. 10), specifically in the case of variable volume. Applying $P_l = 0$ Dirichlet conditions on the liquid sides of the simulation domain would help alleviate this initial pressurized state in the liquid. While the magnitude of the data we have presented here will change under these conditions, we do not expect the trends that we have observed here because of the variable volume to be altered.

V. DISCUSSION AND CONCLUSIONS

Through this paper, homogenous elastic compression is captured, as shown in Fig. 7 according to Eq. (20). Furthermore, the formulation is general enough to input phase and composition-dependent specific volumes which more faithfully reflect real systems with accurate accounting for total

species and strains evolving with composition, as shown in Fig. 10. Variable specific volumes will impact the chemical potentials separately per Eq. (9), such that the construction in Fig. 3 will feature a skew in the potential of the pressurized phase with increasing pressure. Even in the special case of $v_i^\pi = 1$, the lattice constraint is not recovered, unless an incompressible material is assumed.

The inclusion of all species in this paper introduces a new degree of freedom compared with the lattice models, which may be used to control the absolute pressure and chemical potentials of a phase, illustrated in Figs. 6 and 5, respectively. Often, the relative pressure and interdiffusion potential are sufficient outputs when interpreted correctly and the lattice model suffices. However, these factors may become more important with further advances in elastically coupled diffusion where the absolute pressure/state of strain of phases is an important quantity [21].

A key feature of this paper is that the volumetric strain may be described by its local composition per Eq. (15). The representation of the composition is a user choice if the whole composition space is spanned, with the driving force for phase change reflecting the appropriate thermodynamic potential, viz Eq. (24). This presents the possibility of mixed representations, e.g., a combination of concentrations and chemical potentials, N-1 concentrations/chemical potentials combined with the total concentration. This may present a more natural integration with other modeling techniques such as the phase-field crystal method where the total density and N-1 concentrations are considered [41–44].

The model currently only includes homogenous pressure/dilation and incurs stress-driven diffusive flow. Shear stress is an avenue of future development, as is bulk motion driven by deformation or flow which must be recast into an Eulerian frame of reference. Nonetheless, the methodology to represent the homogenous component in a thermodynamically self-consistent fashion is established via the strain energy density in Eq. (8). Therefore, this paper may form a basis for such future efforts.

Here, we have demonstrated the present formulation using free dendritic growth and indeed have shown quantitative differences, particularly in considering constant and variable specific volumes, i.e., variable density. Unfortunately, systematic experimental investigations of free dendritic growth are exceedingly rare. Examples include Refs. [45,46], where the former are experiments done on organic alloys [pivalic acid (PVA)] and the latter on Al-Ge. While the results of the latter contain multiple dendrites and are therefore difficult to compare here, the former on PVA was done in a benchmark study in a microgravity environment to make it convection free and hence effectively eliminate any variation in density. The purpose there was to study the theory of dendritic growth in terms of interface stability and diffusion independently. Such a study with the present formulation is indeed outside the scope here. In that study, they also found, in measuring steady-state tip velocity, those of convection free, i.e., no density variation, to be on average lower than the cases of diffusion-convection transport for all undercooling (Fig. 3 in [45]). This result mirrors what we have found here as well when one looks at the steady-state velocity reached as a function of driving force for constant and variable volume, Fig. 8(b).

Due to the rarity with which such systematic experiments are done, we consider numerical and other theoretical formulations where density/pressure variation is considered during phase transitions to better contextualize the results we have presented and their possible meaning and implications. Such formulations for solidification exist mostly when considering convective fluid flow in examining dendrite settling, motion, or other microstructural effects [47–51]. For example, in Ref. [52], where the kinetics of solute-driven solidification and melting were examined, the authors found that the interface velocity increases due to convection (i.e., variable density) along with changes in segregation. Qi *et al.* [50], in modeling equiaxed dendritic growth coupled to fluid flow and motion, found variation in the steady-state tip velocities of each equiaxed dendrite arm as a function of the different local flow velocities at each encounter (Fig. 4(a) in [50]). Here, the changes in flow velocity leading to the different steady-state tip velocities are aided by the steepness of concentration gradients as determined by pressure and density variations. Finally, in a flow problem examining shrinkage due to density variation, Bhattacharya [49], using an enthalpy-based method, found that shrinkage due to flow generally reduces both steady tip velocities and accumulation of solute ahead of the front, leading to shallower gradients. The results we have just discussed, in terms of physical phenomena, mirror what we have presented here, namely, accounting for density/pressure variation leads to changes in growth rates and accumulation of solute ahead of the growing front. Though we have not accounted for fluid flow, we find that our present model is capable of accounting for and predicting the interesting physical results that up until now were regulated for the involved formulations of flow models. A more thorough examination of free dendritic growth is planned for future work.

In summary, the benefits of the current formulation are

(1) density change via the Helmholtz potential and clear identification of the pressure and Grand potential for the driving force for phase change,

(2) composition- and phase-dependent densification facilitated through inputted specific volumes,

(3) explicit control/calculation of the absolute chemical potential/pressure in phases,

(4) ready generalization to multicomponent systems,

(5) implementation with either c_i or μ_i as dynamic variables,

(6) elimination of implicit contributions to interfacial energies through the Grand potential formulation, and

(7) a point of connection with elastic/fluid models via identification of homogenous dilation/pressure.

Thus, it is shown that, through a proper description of the Helmholtz potential and considering all species compositions in an Eulerian frame of reference, one may capture densification and homogenous elastic stresses in continuum-scale phase-change models. Densification and the flexibility to include phase-dependent specific volumes generalizes the lattice constraint common in other models and fits naturally in the thermodynamic treatment. This approach is derived for isothermal conditions, but an extension to temperature dependence is straightforward. If the interface is also represented with associated interfacial energies, capillary pressure naturally emerges in a general fashion without the need to

alter the composition of coexisting phases. Comparison of this approach with conventional phase-field formulations demonstrates that, while both formulations predict the interdiffusion potential and variation in pressure following classical theory, this approach additionally directly determines the individual quantities and provides a means for user-imposed controls, e.g., the direct control of the pressure of a surrounding phase. The model readily generalizes to multicomponent systems, and the emergence of homogenous dilation/pressure may form a natural point of intersection with elastic/viscoplastic treatments which both identify such a quantity in their description.

ACKNOWLEDGMENTS

The research was funded by Atomic Energy of Canada Limited, under the auspices of the Federal Nuclear Science and Technology Program.

[1] L. I. Rubinstein, *The Stefan Problem* (American Mathematical Society, Providence, 1971).

[2] G. R. Lázaro, I. Pagonabarraga, and A. Hernández-Machado, Phase-field theories for mathematical modeling of biological membranes, Chem. Phys. Lipids. **185**, 46 (2015).

[3] P. Mohammadi, A. S. Aranko, L. Lemetti, Z. Cenev, Q. Zhou, S. Virtanen, C. P. Landowski, M. Penttilä, W. J. Fischer, W. Wagermaier, and M. B. Linder, Phase transitions as intermediate steps in the formation of molecularly engineered protein fibers, Commun. Biol. **1**, 86 (2018).

[4] M. J. Welland, D. Karpeyev, D. T. O'Connor, and O. Heinonen, Miscibility gap closure, interface morphology, and phase microstructure of 3D Li_xFePO_4 nanoparticles from surface wetting and coherency strain, ACS Nano **9**, 9757 (2015).

[5] A. Ulvestad, M. J. Welland, W. Cha, Y. Liu, J. W. Kim, R. Harder, E. Maxey, J. N. Clark, M. J. Highland, H. You, P. Zapol, S. O. Hruszkewycz, and G. B. Stephenson, Three-dimensional imaging of dislocation dynamics during the hydriding phase transformation, Nat. Mater. **16**, 565 (2017).

[6] A. Ulvestad, M. J. Welland, S. S. E. Collins, R. Harder, E. Maxey, J. Wingert, A. Singer, S. Hy, P. Mulvaney, P. Zapol, and O. G. Shpyrko, Avalanching strain dynamics during the hydriding phase transformation in individual palladium nanoparticles, Nat. Commun. **6**, 10092 (2015).

[7] I. Steinbach, Phase-field model for microstructure evolution at the mesoscopic scale, Annu. Rev. Mater. Res. **43**, 89 (2013).

[8] B. Nestler, H. Garcke, and B. Stinner, Multicomponent alloy solidification: Phase-field modeling and simulations, Phys. Rev. E **71**, 041609 (2005).

[9] J. A. Warren and W. J. Boettinger, Prediction of dendritic growth and microsegregation patterns in a binary alloy using the phase-field method, Acta Metall. Mater. **43**, 689 (1995).

[10] M. Plapp, Unified derivation of phase-field models for alloy solidification from a grand-potential functional, Phys. Rev. E **84**, 031601 (2011).

[11] A. Karma, Phase-Field Formulation for Quantitative Modeling of Alloy Solidification, Phys. Rev. Lett. **87**, 115701 (2001).

[12] B. Echebarria, R. Folch, A. Karma, and M. Plapp, Quantitative phase-field model of alloy solidification, Phys. Rev. E **70**, 061604 (2004).

[13] S. G. Kim, A phase-field model with antitrapping current for multicomponent alloys with arbitrary thermodynamic properties, Acta Mater. **55**, 4391 (2007).

[14] C. Tong, M. Greenwood, and N. Provatas, Quantitative phase-field modeling of solidification in binary alloys with nonlinear phase coexistence curves, Phys. Rev. B **77**, 064112 (2008).

[15] M. J. Welland and N. Ofori-Opoku, Simple Method of Including Density Variation in Quantitative Continuum Phase-Change Models, Phys. Rev. Lett. **128**, 075701 (2022).

[16] M. J. Welland, B. J. Lewis, and W. T. Thompson, A comparison of Stefan and phase field modeling techniques for the simulation of melting nuclear fuel, J. Nucl. Mater. **376**, 229 (2008).

[17] M. J. Welland, E. Tenuta, and A. A. Prudil, Linearization-based method for solving a multicomponent diffusion phase-field model with arbitrary solution thermodynamics, Phys. Rev. E **95**, 063312 (2017).

[18] L. Zhang and I. Steinbach, Phase-field model with finite interface dissipation: Extension to multi-component multi-phase alloys, Acta Mater. **60**, 2702 (2012).

[19] M. J. Welland, M. H. A. Piro, S. Hibbins, and N. Wang, A method of integrating CALPHAD data into phase-field models using an approximated minimiser applied to intermetallic layer growth in the Al-Mg system, Calphad **59**, 76 (2017).

[20] M. J. Welland, D. Wolf, and J. E. Guyer, Multicomponent phase-field model for extremely large partition coefficients, Phys. Rev. E **89**, 012409 (2014).

[21] M. J. Welland and S. M. Hanlon, Prediction of the zirconium hydride precipitation barrier with an anisotropic 3D phase-field model incorporating bulk thermodynamics and elasticity, Comput. Mater. Sci. **171**, 109266 (2020).

[22] V. A. Lubarda, Constitutive theories based on the multiplicative decomposition of deformation gradient: Thermoelasticity, elastoplasticity, and biomechanics, Appl. Mech. Rev. **57**, 95 (2004).

[23] A. Choudhury and B. Nestler, Grand-potential formulation for multicomponent phase transformations combined with thin-interface asymptotics of the double-obstacle potential, Phys. Rev. E **85**, 021602 (2012).

[24] M. Hillert, *Phase Equilibria, Phase Diagrams and Phase Transformations: Their Thermodynamic Basis*, 2nd ed. (Cambridge University Press, Cambridge, 2007).

[25] S. G. Kim, W. T. Kim, and T. Suzuki, Phase-field model for binary alloys, Phys. Rev. E **60**, 7186 (1999).

[26] C. H. P. Lupis, *Chemical Thermodynamics of Materials* (North-Holland, New York, 1983).

[27] S. R. de Groot and P. Mazur, *Non-Equilibrium Thermodynamics* (Dover Publications, New York, 1984).

[28] M. J. Welland, Matter Transport in Fast Reactor Fuels, in *Comprehensive Nuclear Materials*, 2nd ed., edited by R. Konings, and R. E. Stoller, (Elsevier, Oxford, 2020), Vol. 2, Chap. 8, pp. 200–247.

[29] M. J. Welland, W. T. Thompson, B. J. Lewis, and D. Manara, Computer simulations of non-congruent melting of hyperstoichiometric uranium dioxide, J. Nucl. Mater. **385**, 358 (2009).

[30] M. J. Welland, Introduction to the phase-field modelling technique: A primer on the Allen-Cahn and Cahn-Hilliard models, in *State-of-the-Art Report on Multi-Scale Modelling Methods*, Report No. NEA/NSC/R(2019)2, (Nuclear Energy Agency of the OECD (NEA), 2020), Chap. 8, pp. 128–142.

[31] COMSOL Multiphysics Reference Manual Version 5.5 COMSOL, Inc., Burlington, (2019).

[32] A. Logg and G. N. Wells, DOLFIN: Automated finite element computing, ACM Trans. Math. Softw. **37**, 1 (2010).

[33] A. Logg, K.-A. Mardal, and G. Wells, editors, *Automated Solution of Differential Equations by the Finite Element Method* (Springer Berlin Heidelberg, Berlin, Heidelberg, 2012), Vol. 84.

[34] R. C. Kirby and A. Logg, A compiler for variational forms, ACM Trans. Math. Softw. **32**, 417 (2006).

[35] M. S. Alnæs, A. Logg, K. B. Ølgaard, M. E. Rognes, and G. N. Wells, Unified form language: A domain-specific language for weak formulations of partial differential equations, ACM Trans. Math. Softw. **40**, 1 (2014).

[36] Chapter 6.6, "Effect of a pressure difference on a two-phase equilibrium."

[37] M. M. Demin, O. N. Koroleva, A. A. Aleksashkina, and V. I. Mazhukin, Molecular-dynamic modeling of thermophysical properties of phonon subsystem of copper in wide temperature range, Math. Montisnigri **47**, 137 (2020).

[38] R. N. Abdullaev, Yu. M. Kozlovskii, R. A. Khairulin, and S. V. Stankus, Density and thermal expansion of high purity nickel over the temperature range from 150 K to 2030 K, Int. J. Thermophys. **36**, 603 (2015).

[39] D. R. Poirier and G. H. Geiger, *Transport Phenomena in Materials Processing* (Springer International Publishing, Cham, 2016).

[40] N. Ofori-Opoku and N. Provatas, A quantitative multi-phase field model of polycrystalline alloy solidification, Acta Mater. **58**, 2155 (2010).

[41] N. Ofori-Opoku, V. Fallah, M. Greenwood, S. Esmaeili, and N. Provatas, Multicomponent phase-field crystal model for structural transformations in metal alloys, Phys. Rev. B **87**, 134105 (2013).

[42] B. A. Jugdutt, N. Ofori-Opoku, and N. Provatas, Calculating the role of composition in the anisotropy of solid-liquid interface energy using phase-field-crystal theory, Phys. Rev. E **92**, 042405 (2015).

[43] M. J. Frick, N. Ofori-Opoku, and N. Provatas, Incorporating density jumps and species-conserving dynamics in XPFC binary alloys, Phys. Rev. Materials **4**, 083404 (2020).

[44] M. Greenwood, N. Ofori-Opoku, J. Rottler, and N. Provatas, Modeling structural transformations in binary alloys with phase field crystals, Phys. Rev. B **84**, 064104 (2011).

[45] J. C. Lacombe, M. B. Koss, and M. E. Glicksman, Tip velocities and radii of curvature of pivalic acid dendrites under convection-free conditions, Metall. Mater. Trans. A **38**, 116 (2007).

[46] M. Becker, S. Klein, and F. Kargl, Free dendritic tip growth velocities measured in Al-Ge, Phys. Rev. Materials **2**, 073405 (2018).

[47] D. Tourret, M. M. Francois, and A. J. Clarke, Multiscale dendritic needle network model of alloy solidification with fluid flow, Comput. Mater. Sci. **162**, 206 (2019).

[48] C. Beckermann, H.-J. Diepers, I. Steinbach, A. Karma, and X. Tong, Modeling melt convection in phase-field simulations of solidification, J. Comput. Phys. **154**, 468 (1999).

[49] A. Bhattacharya, Binary alloy dendrite growth in presence of shrinkage induced convection, Mater. Res. Express **6**, 126544 (2019).

[50] X. B. Qi, Y. Chen, X. H. Kang, D. Z. Li, and T. Z. Gong, Modeling of coupled motion and growth interaction of equiaxed dendritic crystals in a binary alloy during solidification, Sci. Rep. **7**, 45770 (2017).

[51] C. Beckermann, Modeling segregation and grain structure development in equiaxed solidification with convection, JOM **49**, 13 (1997).

[52] E. Gamsjäger, J. Svoboda, F. D. Fischer, and M. Rettenmayr, Kinetics of solute driven melting and solidification, Acta Mater. **55**, 2599 (2007).